Applied Materials Today 36 (2024) 102033

Contents lists available at ScienceDirect

Applied Materials Today

journal homepage: www.elsevier.com/locate/apmt

Spatially selective crystallization of ferroelectric $Hf_{0.5}Zr_{0.5}O_2$ films induced by sub-nanosecond laser annealing

Alejandro Frechilla [a,b], Mari Napari [c,d,e,1], Nives Strkalj [c], Eduardo Barriuso [a], Kham Niang [f], Markus Hellenbrand [c], Pavel Strichovanec [a], Firman Mangasa Simanjuntak [e], Guillermo Antorrena [a,g], Andrew Flewitt [f], César Magén [a,h], Germán F. de la Fuente [a], Judith L. MacManus-Driscoll [c], Luis Alberto Angurel [a,b], José Ángel Pardo [a,b,g,*]

[a] Instituto de Nanociencia y Materiales de Aragón, CSIC - Universidad de Zaragoza, C/ María de Luna 3, 50018 Zaragoza, Spain
[b] Departamento de Ciencia y Tecnología de Materiales y Fluidos, Universidad de Zaragoza, C/ María de Luna 3, 50018 Zaragoza, Spain
[c] Department of Materials Science & Metallurgy, University of Cambridge, 27 Charles Babbage Road, Cambridge CB3 0FS, United Kingdom
[d] Zepler Institute, University of Southampton, Southampton SO17 1BJ, United Kingdom
[e] School of Electronics and Computer Science, University of Southampton, Southampton SO17 1BJ, United Kingdom
[f] Engineering Department, University of Cambridge, Trumpington Street, Cambridge CB2 1PZ, United Kingdom
[g] Laboratorio de Microscopías Avanzadas, Universidad de Zaragoza, Campus Río Ebro, 50018 Zaragoza, Spain
[h] Departamento de Física de la Materia Condensada, Universidad de Zaragoza, 50009 Zaragoza, Spain

ARTICLE INFO

Keywords:
Ferroelectricity
Hafnia
Crystallization
Laser processing

ABSTRACT

In this work we study the sub-nanosecond laser-induced crystallization of 10 nm-thick atomic layer deposited amorphous $Hf_{0.5}Zr_{0.5}O_2$ (HZO) films in an air atmosphere. We used an infrared laser with 1064 nm wavelength and 800 ps pulses to anneal TiN/HZO/TiN capacitors by scanning an 80 μm-diameter spot along their top surface in a controlled way. The laser annealing process was optimised in terms of fluence to achieve the complete crystallization of HZO into a non-monoclinic polymorph, as demonstrated by X-ray diffraction and transmission electron microscopy. Piezoresponse force microscopy and polarization-field loops confirm that the optimal as-annealed HZO films are piezoelectric and ferroelectric from the first cycle on. Spatial selectivity was accomplished by scanning the laser on selected areas of the samples. Micro-diffraction experiments show that the transition between the crystallized and the amorphous region is abrupt within a distance of several hundred μm.

1. Introduction

The discovery of ferroelectricity in Si-doped HfO_2 films in 2011 [1] opened up a large research effort about the nature and application of this phenomenon in pure and doped hafnium oxide, zirconium oxide and their respective solid solutions, with $Hf_{0.5}Zr_{0.5}O_2$ being the most widely studied composition [2–3]. HfO_2 and ZrO_2 have fluorite-related crystal structures and show complete solubility. Several polymorphs are stable in thermodynamic equilibrium at different temperatures, from the high-temperature cubic *Fm*-3*m* to the room-temperature monoclinic $P2_1/c$ through the intermediate tetragonal $P4_2/nmc$ [4]. However, a non-equilibrium ferroelectric phase which belongs to the non-centrosymmetric orthorhombic $Pca2_1$ space group [5] is kept in a metastable state through surface energy contributions, impurities, vacancies or strain.

The huge technological interest of hafnia is boosted by its chemical simplicity compared with other ferroelectrics and its compatibility with CMOS technology, with a well-established use of similar compositions in the microelectronics industry as a dielectric with high permittivity, large bandgap, high breakdown field and superior thermal stability. A large number of recent publications report on the applications of ferroelectric hafnia in devices for energy conversion/storage or computing: supercapacitors, non-volatile random-access memories, ferroelectric field-effect transistors, ferroelectric tunnel junctions, memristors, or negative capacitance transistors [6–16].

The development of next-generation devices based on ferroelectrics requires not only materials with a range of desired properties but also new fabrication methods to allow the patterning of submillimetre

* Corresponding author at: Instituto de Nanociencia y Materiales de Aragón, CSIC - Universidad de Zaragoza, C/ María de Luna 3, 50018 Zaragoza, Spain.
E-mail address: jpardo@unizar.es (J.Á. Pardo).
[1] Present address: Department of Physics, King's College London, London WC2R 2LS, United Kingdom

https://doi.org/10.1016/j.apmt.2023.102033
Received 31 July 2023; Received in revised form 29 November 2023; Accepted 15 December 2023
Available online 23 December 2023

structures. The standard procedure to prepare basic capacitors containing ferroelectric hafnia sandwiched between two metallic electrodes is the sequential deposition of the component layers in amorphous thin film form followed by crystallisation by rapid thermal annealing (RTA) [2–3]. The latter process is most often done in a nitrogen-rich environment at temperatures in the range 500–1000 °C for several minutes or tens of seconds [17,18], which involves a high thermal budget. These process features help to create the metastable orthorhombic ferroelectric phase, by producing thermal stress from the electrodes and oxygen vacancies from the oxygen-deficient atmosphere [17,18]. Alternative methods to the RTA process, based on the use of flash lamps [17,19,20], lasers [21–27], or ion irradiation [28] have recently demonstrated advantages towards the formation of the non-equilibrium orthorhombic polymorph and deserve further consideration.

Laser processing methods are widely implemented in the industry because of their easy scalability and environmentally friendly character (low energy consumption, few chemical products, etc.). They allow superior control of the delivered energy and of the size and shape of the irradiated region. In addition, they exhibit high processing speeds and generate extremely fast heating and cooling rates, which open the possibility of quenching non-equilibrium metastable phases. The effects associated to pulsed laser irradiation of materials, including the penetration depth, can be controlled by selecting the wavelength, pulse duration, repetition frequency, fluence (pulse energy per surface area) and irradiance (fluence per unit time), as well as the number of pulses. In the particular case of ultrashort pulsed lasers, the lateral spread of the thermally affected volume depends on the size of the focused beam and on the thermal properties of the processed material [29,30]. Such laser annealing allows the spatially selective transformation of particular areas to be induced while preserving the adjacent regions from being heated or damaged. Similar approaches have been used before to induce the crystallization of ferroelectric glasses [31] or to write electronic circuitry through structural or chemical phase transformations [32], and could be a promising strategy to integrate the crystallization of HZO into the fabrication of devices.

Few studies on pulsed laser annealing (PLA) of hafnia-based films have been published to date. They are summarized in Table 1. In most cases, surface areas of around 1 cm^2 of pure or doped HfO_2 or ZrO_2 films were crystallized by cumulative irradiation with a high enough number of pulses of an ultraviolet (UV) excimer laser [21,22,24–27]. In one instance, an infrared (IR) laser with 16 ns or 1 ms pulses focused into a spot with 0.2 or 1 mm of diameter was used to transform partially some regions of $Hf_{0.5}Zr_{0.5}O_2$ films through the deposition of reflecting metallic masks [23]. Those publications confirm that large areas of as-deposited amorphous hafnia films can become ferroelectric after annealing with lasers of very different wavelengths (in the UV or IR range) and pulse durations. They do not explore, however, the possible intrinsic spatial selectivity of the technique. This is because the relative positions of the sample and the laser beam are static, the illuminated areas typically exhibit sizes within the tens of mm^2 range, and apply pulse duration values between tens of ns and 1 ms, thus involving large heat-affected zones.

In this paper we address the sub-nanosecond laser-induced crystallization of 10 nm-thick $Hf_{0.5}Zr_{0.5}O_2$ (HZO) films in a parallel-plate capacitor geometry with TiN electrodes, deposited on 1×1 cm^2 thermally oxidized Si substrates. The as-deposited HZO films are amorphous,

Table 1
Summary of previous publications on laser-induced crystallisation of hafnia-based films compared to the present work.

Reference	Composition of the films and substrate. Thickness of ferroelectric film	Laser type (wavelength) and pulse duration	Laser annealing method	Laser beam size at the working distance. Fluence per pulse	Number of pulses per position. Repetition frequency. Atmosphere	Spatial selectivity	Remarks
Song et al. [27]	TiN/HZO/TiN on n-type Si (several Hf/Zr ratios). 8–16 nm	KrF (248 nm) 20 ns	Repetitive spots on the same position. No scanning	50 mm^2. 0.07 J/cm^2	10, 50, 100, 500, and 1000 pulses. 10 Hz. Air atmosphere	No	Laser annealing of HZO before the deposition of TiN top electrode
Crema et al. [26]	W/ZrO_2/W on p-type Si/SiO_2. 8 nm	KrF (248 nm) 25 ns	Repetitive spots on the same position. No scanning	10×5 mm^2 (larger than the sample). 0.4 J/cm^2	100 pulses. 10 Hz. Air atmosphere	No	Comparison of laser annealing on samples with and without W top electrode
Tabata [21]	TiN/HfO_2 on Si and Si/SiO_2. 50 nm	XeCl (308 nm) 100–200 ns	Repetitive spots on the same position. No scanning	Illuminated area larger than the sample. Fluence not given	1, 5, 10 and 100 pulses. Repetition frequency not given. N_2 atmosphere	No	Ferroelectric switching not confirmed
Grenouillet et al. [22]	TiN/Si:HfO_2/TiN on Si/SiO_2. 10 nm	XeCl (308 nm) 160 ns	Repetitive spots on the same position. No scanning	Not specified. 0.1–0.5 J/cm^2	1, 10 and 100 pulses Repetition frequency and atmosphere not given	No	Gradual transition
Ali et al. [25]	TiN/Si:HfO_2/TiN on B:Si. 10 nm	XeCl (308 nm) 160 ns	Repetitive spots on the same position. No scanning	10×10 mm^2. 0.3–1.3 J/cm^2	1–30 pulses. Repetition frequency not given. N_2 atmosphere	No	Fluence threshold for crystallization determined (0.75 J/cm^2)
Tabata et al. [24]	TaN/HfO_2 on n-type Si. 10 nm	UV laser (300–400 nm). Pulse duration not given	(Not specified)	(Not specified)	(Not specified)	(Not expected)	Laser annealing without a top electrode
Volodina et al. [23]	W/HZO/TiN on Si or Al_2O_3 10 nm	Nd:YAG (1064 nm) 1 ms / 16 ns	Beam scanning. Scanned area: 5×10 mm^2	Circular with a diameter of 200 μm or 1000 μm. 120 J/cm^2	Scanning. Repetition frequency not given. Vacuum (10^{-7} mbar)	Yes, through the use of reflecting masks	Crystallization obtained only with 1 ms pulses
This work	TiN/HZO/TiN on Si/SiO_2 10 nm	Nd:YAG (1064 nm) 800 ps	Laser line scanning. Scanned area: 10×10 mm^2	Circular with a diameter of 80 μm. 0.05–0.16 J/cm^2	Scanning, 50 pulses (1D), 4021 pulses (2D). 800 kHz. Air atmosphere	Yes	Sharp transition

and thus non-ferroelectric. We use a near infrared laser with a pulse duration of 800 ps and an output wavelength of 1064 nm to anneal the capacitors through a line scanning approach [33,34], in which an 80 μm diameter spot of the focused laser scans the whole surface of a TiN/HZO/TiN stack under an air atmosphere. The process takes less than 4 min.

Under optimised conditions of laser fluence, it is found that there is complete crystallization of the HZO film and the formation of a non-monoclinic polymorph (as determined by X-ray diffraction and transmission electron microscopy). Also, the films are piezoelectric and ferroelectric, as determined by piezoresponse force microscopy and polarization-field loops. Next, it is found that the same laser processing performed on just one half of the surface area (0.5×1 cm^2) of a square sample enables selective crystallisation (as determined by micro-diffraction experiments). Furthermore, the transition between non-ferroelectric and ferroelectric regions is steep within a few hundreds of microns.

Our approach paves the way for the integration of ferroelectric hafnia on devices through the spatially selective crystallization by pulsed laser patterning. In addition, it is fast and enables low thermal budget processing of samples.

2. Methods

40 nm-thick TiN electrodes were deposited on silicon wafers with a 200 nm thermal silicon oxide layer by reactive sputtering (Angstrom Engineering) at room temperature using a Ti target and nitrogen plasma (20 sccm, 600 W). A 10 nm HZO film was then deposited on the TiN (bottom electrode) by atomic layer deposition (ALD, Veeco Nanotech Savannah S200) at 200 °C using tetrakis(dimethylamino)hafnium (TDMAH, $Hf[(CH_3)_2N)]_4$, Sigma-Aldrich), tetrakis(dimethylamino)zirconium (TDMAZ, $Zr[(CH_3)_2N)]_4$, Sigma-Aldrich) and H_2O. The TDMAH and TDMAZ precursors were sublimed at 75 °C and 70 °C, respectively, and the H_2O was kept at room temperature. The chamber pressure was set to 0.6 Torr by 90 sccm Ar flow, which also served as a carrier gas for the precursor delivery. To enhance the TDMAH delivery to the deposition chamber, Ar was released to the precursor container via a boost valve prior to each precursor pulse. The HZO layer was deposited by alternating HfO_2 and ZrO_2 ALD cycles (1:1 HfO_2:ZrO_2), where each cycle consisted of 0.2 s TDMAH or TDMAZ / 8 s purge / 0.02 s H_2O / 8 s purge. For 10 nm HZO films, a total of 100 cycles were deposited (50 HfO_2, 50 ZrO_2). Another 40 nm-thick TiN layer (top electrode) completed the TiN/HZO/TiN stack.

A pulsed Nd:YAG laser (PowerLine Pico from Rofin, Germany) with a maximum power of 8 W, emitting 800 ps pulses at a wavelength of 1064 nm, was employed for the laser processing experiments. These were carried out in air atmosphere following the laser line scanning approach [35]. The laser was operated at a pulse repetition frequency of 800 kHz, and the Gaussian beam was focused with optical lenses into an 80 μm diameter spot. The system was equipped with galvanometer mirrors so that the spot could define a 1-dimensional (1D) scan at a given velocity along the surface of the sample. This configuration generates a uniform heat front on the film surface, which is then combined with the movement of the sample in the perpendicular direction at a constant velocity, thus defining a 2-dimensional (2D) scan of the selected region. All the examples presented in this work were processed with a laser scanning speed of 1000 mm/s, and 150 mm/h of transverse speed. The different levels of the laser treatment were selected by modifying the energy per pulse, $E_{pulse}=P/f$, where P is the laser power and f is the frequency. The relationship between E_{pulse} and the total energy density at the sample during the laser scan can be derived following the calculations presented in Reference [36]. During the 1D scan, the effective number of pulses in each position, defined as the ratio between the total energy density deposited on the surface and the pulse fluence, is 50 pulses. This number increases to 4021 pulses, when the 2D scan is considered. It is important to have in mind that the time scales for the 1D and 2D scans are very different, μs in 1D and 10 ms in 2D.

The TiN top electrode was removed from the laser-processed TiN/HZO/TiN trilayers by reactive ion etching (Sistec) with a 20 sccm flow of SF_6 gas and 200 W of RF power. The process duration was optimised to selectively remove the TiN while leaving the HZO unaffected, as demonstrated with profilometry and transmission electron microscopy (TEM). Electron beam evaporation (Boc Edwards) and stencil masks were then used to deposit a matrix of square pads with 100×100 μm^2 size and 20 μm separation, consisting of a 20 nm-thick layer of Cr on the bare HZO film as an adhesion layer, and a 200 nm-thick Au layer on top. The pressure during the evaporation was 1×10^{-6} mbar for Cr and 5×10^{-6} mbar for Au. The deposition rate was 5 nm/min for Cr and 8 nm/min for Au. Fig. 1 summarizes the procedure described in these paragraphs.

The structural characterization of 1×1 cm^2 samples before and after laser processing was done by X-ray diffraction (XRD) in Bragg-Brentano geometry using a PANalytical Empyrean system. To collect the entire signal from the film in the 25–40° range of the detector angle, while avoiding the strong reflection of the single-crystal Si substrate at $2\theta = 33.1°$, the incidence angle (omega, ω) was deliberately tilted by 2° away from the symmetric position.

The micro-diffraction (μXRD) experiments were performed in a PANalytical X'Pert PRO MRD diffractometer with parallel beam optics (divergence below 0.04°) giving a very narrow beam with 80 μm of equatorial width and 14 mm of axial length. The sample position was aligned carefully so that the visual interface between the pristine and the laser-processed zones was located in the goniometer centre with an estimated accuracy of ±0.1 mm in X and Y, and ±5 μm in Z, and a maximum deviation of 0.5° in parallelism between Y and the apparent boundary. To reduce the contribution of X-ray scattering in the air and thus improve the peak-to-background ratio, a beam knife was placed at a distance of less than 1 mm from the goniometer centre and the surface of the sample. Diffractograms were taken at 2θ values from 25° to 40° at a constant incident angle of $\omega = 24°$, which gives a projected equatorial size of the beam on the sample of 200 μm. Several 2θ scans were acquired at different values of the X coordinate. Additional measurements were taken by fixing 2θ and scanning the X position in steps of 50 μm. Both diffractometers used Cu-Kα radiation (1.5418 Å wavelength) and PIXcel® array detectors.

X-ray photoelectron spectroscopy (XPS) was measured in selected samples with a Kratos Axis Supra equipment using Al Kα radiation (1486.6 eV). The lateral size of the region explored was 0.7×0.3 mm^2. The spectra were charge-corrected to the main line of the carbon 1s spectrum (adventitious carbon) set to 284.8 eV, and analysed using the CasaXPS software, including the subtraction of a Shirley baseline for the background.

The local microstructure of the films was analysed by scanning transmission electron microscopy (STEM) and high-resolution transmission electron microscopy (HRTEM) of electron-transparent cross-sectional lamellas prepared by focused ion beam (FIB) milling using a Helios NanoLab 600 SEM-FIB microscope. STEM analysis was performed in a probe-corrected FEI Titan 60–300 microscope, operated at 300 kV, and equipped with a high-brightness field emission gun (X-FEG) and a CEOS aberration corrector for the condenser system. High-angle annular dark field (HAADF) imaging was performed in STEM, with a convergence semi-angle of 24 mrad and a probe size below 1 Å. Chemical composition maps were obtained by X-ray energy dispersive spectroscopy (EDS) with an Ultim Max TLE 100 silicon drift detector from Oxford Instruments. HRTEM images were also collected in the Titan Low Base at 300 kV with a Gatan Ultrasan CCD camera.

The thin-film topography and piezoresponse were measured using a Bruker Multimode 8 atomic force microscope (AFM) in air. Piezoresponse force microscopy and spectroscopy (PFM and PFS) measurements were performed with Pt-coated NSC35 tips (MikroMasch) and the PFM contrast was recorded in polar coordinates.

An AixACCT TFAnalyser2000 was used to measure ferroelectric

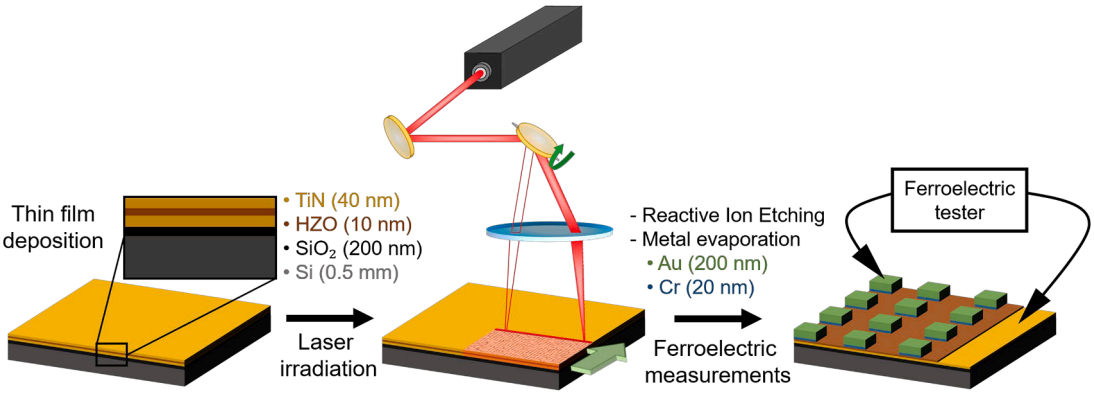

Fig. 1. Schematic illustration of the deposition, laser-induced crystallization and subsequent processing of the HZO thin films. See the text for explanations.

polarization loops and endurance at room temperature in the configuration with a grounded bottom TiN electrode and a bias application at the top Cr/Au electrode. Ferroelectric polarization loops and endurance were obtained in dynamic hysteresis measurement mode at a frequency of 1 kHz by integrating the current response. The endurance was evaluated using bipolar pulses at 100 kHz and by measuring the hysteresis loops at 1 kHz at five points in a decade.

3. Results and discussion

In the first series of experiments, eight nominally identical TiN/HZO/TiN film samples with 1×1 cm^2 size were fully annealed through the single 2D process described above. All the laser annealing processes were carried out in air under atmospheric conditions. The energy per pulse was varied between samples within the 2.52–7.86 μJ/pulse range. Fig. 2 shows the XRD patterns measured in these films, together with one corresponding to an as-deposited sample.

As observed in Fig. 2, laser annealed films obtained at energy per pulse values below 3.93 μJ/pulse exhibit only one line at 2θ ≈ 36.7°, indexed as the (111) reflection of cubic δ-TiN with lattice parameter of 4.24 Å [37], corresponding to the top and bottom electrodes. This indicates that the HZO films remain amorphous at lower laser energies. Films processed slightly above the 3.93 μJ/pulse level (*i.e.* at 4.30 μJ/pulse and 5.50 μJ/pulse) exhibit additional reflections at 2θ = 30.8° and 2θ = 35.6°. The first of these can be attributed to either the $P4_2/nmc$ tetragonal (101) or the polar orthorhombic (111) structure of HZO,

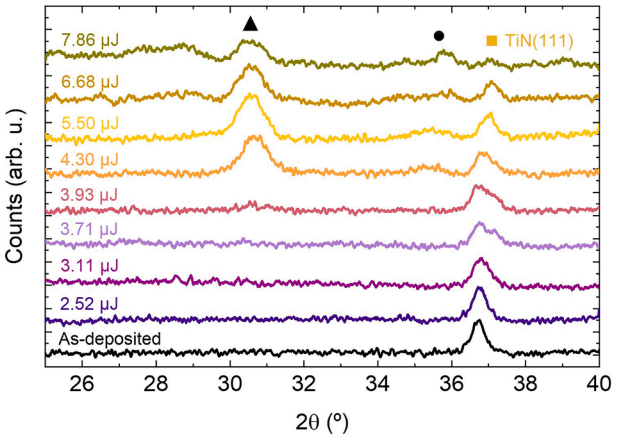

Fig. 2. XRD patterns of laser-annealed TiN/HZO/TiN trilayers for different energies per pulse, compared to an as-deposited sample. The full triangle shows the expected position of the 101 reflection of the tetragonal phase or the 111 reflection of the polar, orthorhombic phase. The full circle could correspond to several polymorphs (see the text for details).

while the second is compatible with all its known polymorphs. The monoclinic phase, whose most intense reflections appear at 2θ values around 28.5° (11–1) and 32° (111), was not detected in these samples. Therefore, it can be confirmed that a non-equilibrium polymorph is formed for these two values of the laser energy per pulse.

Quite remarkably, the shape, intensity and width of the XRD line at 2θ = 30.8° remains constant, to within the experimental accuracy, for 4.30 and 5.50 μJ/pulse. This phenomenon suggests an "on-off" crystalline transition. For all laser energies and using the 30.8° line, the average crystallite size along the thickness direction, determined from Scherrer's semi-empirical equation was 10.6 ± 0.7 nm, a value similar to the film thickness. This confirms that the crystallization of the particular phase which gives rise to the 30.8° line, along the out-of-plane direction, is complete at 4.30 μJ/pulse. However, as the laser energy increases above 5.50 μJ/pulse, it is observed that the line at 30.8° gradually reduces with increasing energy, while a broad band in the range 28–29° and low-intensity lines at 2θ angles around 36° and above begin to emerge. These lines could correspond to the monoclinic phase, although their low intensity hindered an unambiguous identification.

It is worth mentioning that the XRD reflection corresponding to TiN around 2θ ≈ 36.7° splits in two smaller lines for increasing values of laser energy. A small bump at the high-angle side can be seen for pulse energies of 3.71 μJ/pulse and larger. Its relative contribution to the doublet increases with increasing laser energy per pulse, and becomes dominant (peak at 2θ ≈ 37°) above 5.50 μJ/pulse. This could be an indication of the partial oxidation of titanium nitride from the top electrode in contact with the ambient atmosphere, as has been reported to occur by laser annealing of TiN in air [38,39]. Nevertheless, the partial oxidation of both TiN electrodes and the formation of an oxide or oxynitride through the scavenging of oxygen from adjacent SiO_2 or HZO as a result of local heating is also feasible in our films, as reported before [40–42]. The lattice parameter of cubic $TiN_{1-\delta}O_\delta$ with rock-salt crystal structure ranges between 4.24 Å for TiN (corresponding to 2θ ≈ 36.7°) [37] and 4.20 Å for TiO (corresponding to 2θ = 37.0°) [43]. The possible oxidation of TiN close to the interfaces with HZO would result in a concomitant partial reduction of HZO, thus generating a small amount of oxygen vacancies and a slight increase in the lattice parameters (given the larger size of trivalent cations relative to tetravalent ones), which would produce a shift in the diffraction peaks. Indeed, a subtle decrease in the 2θ value of the maximum from 30.8° to ≈30.7° can be observed for increasing the energy per pulse above 4.30 μJ. Nevertheless, detailed studies correlating the laser annealing conditions, oxygen vacancy distribution and crystal structure with spatial resolution would be needed to confirm this explanation, which is beyond the scope of this paper. At the highest energy explored (7.86 μJ/pulse), in addition to the strongest HZO reflection decreasing in intensity, so does the main $TiN_{1-\delta}O_\delta$ line at 2θ ≈ 37°. This is compatible with the formation of other titanium oxides at higher fluence values, as reported by [39]. Thus, all the materials in the stack seem to degrade.

Overall, the sample processed with a pulse energy of 4.30 μJ/pulse appears to have induced complete crystallisation of HZO and no marked degradation of the TiN electrodes. These conditions were hence considered optimum. Furthermore, the XRD patterns appeared identical when different samples were annealed under the same laser parameters, confirming the reproducibility of the process (see Supplementary Fig. S1). Consequently, the following experiments for the structural, compositional and physical characterization were conducted on these films.

To explore possible lateral gradients of composition in these HZO films or changes of stoichiometry induced by the laser annealing, we conducted XPS experiments in identical samples before and after the irradiation with 4.30 μJ of energy per pulse. In both cases the TiN top electrode was removed by RIE prior to the measurement so that bare HZO could be probed directly. Supplementary Fig. S2 a) shows survey spectra measured in three different regions distant several millimetres of an annealed sample. As it can be seen, almost identical results were obtained, confirming the lateral homogeneity of the laser-processed HZO film. Fig. S2 b) and c) present high-resolution spectra around the Hf 4f and Zr 3d bands, respectively, measured in the films before and after laser irradiation. The minor differences between samples prove that there is no substantial change of stoichiometry associated to the laser crystallisation. In particular, we could not confirm the presence of Hf^{3+} or Zr^{3+} in the depth explored, within the experimental accuracy [40–42]. This could indicate that the oxygen vacancies suggested by our XRD analysis would be located close to the interface with the TiN bottom electrode, or that the higher atomic layers of HZO get fully oxidized by the atmosphere after etching of the TiN top electrode. The use of hard X-rays [42] or angle-resolved XPS [40] could help clarify these hypotheses.

TEM analysis of the microstructure and chemistry of the sample processed with these parameters is illustrated in Fig. 3. In particular, the specimen studied here had the top TiN layer etched away, and Cr/Au contacts deposited on the HZO. HAADF-STEM imaging of the HZO film and its interfaces with the TiN (bottom) and the Cr (top) layers shown in Fig. 3(a) demonstrates the HZO film thickness homogeneity along tens of nanometres. Its crystalline nature is confirmed by HRTEM of the same sample (Fig. 3(b)), where lattice fringes of the HZO crystallites can be

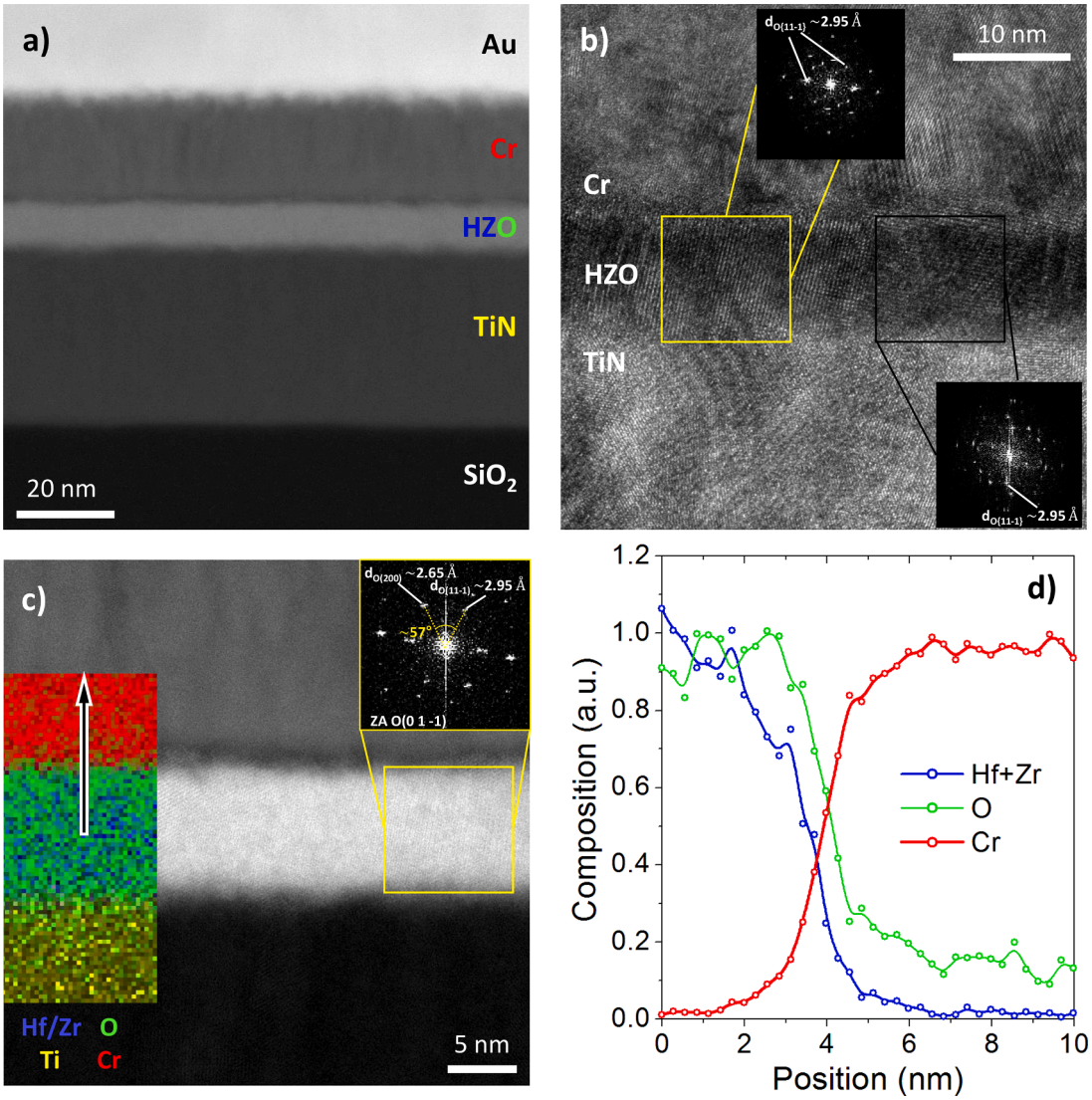

Fig. 3. **a)** Low-magnification HAADF-STEM image of a cross-sectional specimen of the optimal laser-annealed sample, after the removal of top TiN and the deposition of a Cr/Au electrode. **b)** HRTEM image of the TiN/HZO/Cr region in the same sample. **c)** High magnification HAADF-STEM image of the region of the specimen, similar to the one shown in b), where STEM-EDS chemical mapping has been performed. Indexed local fast Fourier transforms of specific grains are shown in b) and c). The inset in c) represents the colour-coded EDS map of TiN/HZO/Cr region (Hf+Zr in blue, O in green, Cr in red, Ti in yellow). **d)** Chemical profiles (in arbitrary units, normalized to the average value of each species within the corresponding layer) of Hf+Zr, O and Cr. (For interpretation of the references to color in this figure legend, the reader is referred to the web version of this article.)

seen intermixed with the neighbouring layers, and by HAADF-STEM with higher magnification (Fig. 3(c)). The HZO film is indeed polycrystalline, with no clear indication of amorphous regions, and with a grain size comparable to the film thickness, in agreement with the XRD results. The overlapping of the small crystallites with random orientations throughout the lamella thickness, and the similarity of the crystal lattice of the possible HZO polymorphs precludes the precise identification of the phases present in most regions. However, some grains can be found properly oriented for indexation. For instance, local fast Fourier transforms (FFT) of the images in Fig. 3b) and c) indicate the presence of orthorhombic grains, identified by their {111} family of planes, with interplanar distance of ~2.95 Å. The gradual contrast change across the HZO interfaces is indicative of the significant roughness caused by the polycrystalline nature of the heterostructure. Figure S3 of the Supplementary Information illustrating the HAADF-STEM images and chemical analysis of a TiN/HZO/TiN cross-sectional specimen proves that the same conclusions are valid before the removal of TiN top electrode. The EDS chemical maps depicted in Fig. 3 (d) show that the HZO film is compositionally homogeneous. The chemical line profile across the HZO/Cr interface indicates an interface depth of ~2 nm, which is coherent with the observed interfacial roughness. The slight shift (~0.6–0.8 nm) of the Hf+Zr profile relative to the O profile cannot be explained by roughness effects. Due to the high oxygen affinity of Cr, it is reasonable to interpret this mismatch as the partial oxidation of Cr near the HZO film, as previously observed in HfO_2/Cr interfaces [44]. Nevertheless, although the chamber pressure during the evaporation of Cr was 10^{-6} mbar, any physisorbed OH on the surface of HZO could have also induced some degree of oxidation of the Cr layer.

From AFM, a surface roughness of 0.8 nm was found for a bare HZO film (after etching of the top TiN electrode) annealed with 4.30 μJ/pulse (Fig. 4(a)). Lines of 1 nm height with about 100 nm spacing were detected. Additionally, sparse grains with spacings of several microns, 10 nm height and 500 nm diameter, were found on top of the HZO layer which are likely attributable to the etching. From PFM measurements (locally applied V_{dc} of ±10 V to the sample while grounding the PFM tip followed by reading the response at V_{ac} of 2 V at 15 kHz), switching was observed, as shown in Fig. 4(b). The presence of two contrast levels in the PFM out-of-plane phase and small amplitude changes after the application of an electric field suggests the presence of reversibly switchable polarization, *i.e.* ferroelectricity. Furthermore, a signal dip in PFM amplitude is observed at positions of phase contrast change and attributed to the presence of domain walls [45]. We additionally performed PFS scans out-of-plane at positions forming a 5×5 matrix with 500 nm spacings (Figs. 4(c) and 4(d)). All points show a typical ferroelectric response in amplitude and phase with a coercive field of (2.3 ± 0.5) MV/cm.

To assess the remanent polarization, coercive field and endurance of the TiN/HZO/Cr/Au devices, a ferroelectric tester was used. A remanent polarization is observed from the first cycle on, increases in amplitude up to 10^4 cycles, suggesting an increase in ferroelectric phase content, and stays constant up until dielectric breakdown which typically occurs at around 10^4–10^5 cycles, see Fig. 5(a) and Supplementary Fig. S4. Dielectric breakdown is also induced when the field amplitude exceeds 4–5 MV/cm, as shown in field-amplitude-dependent measurements in Supplementary Figure S5. In the current-density-field representation of

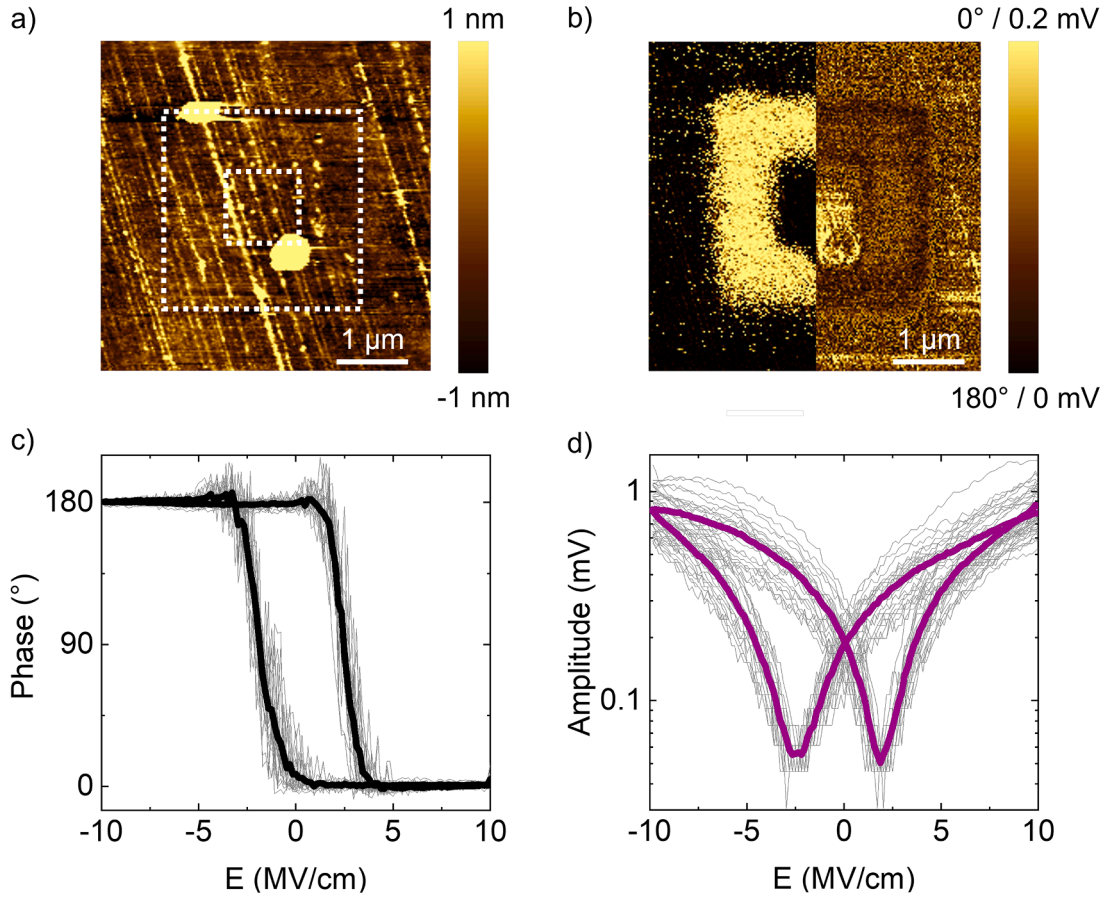

Fig. 4. **a)** Topography of laser-annealed HZO films measured by AFM. **b)** PFM out-of-plane response collected with V_{ac} of 2 V in phase (left half) and amplitude (right half) after poling a 3×3 μm^2 area with V_{dc} of 10 V and then poling a centred 1×1 μm^2 area with V_{dc} of −10 V. **c and d)** PFS out-of-plane scans in **c)** phase and **d)** amplitude collected with V_{ac} of 2 V at positions forming a 5×5 matrix with 500 nm spacings are shown in grey. Average phase and amplitude measurements are shown in black and purple, respectively. (For interpretation of the references to color in this figure legend, the reader is referred to the web version of this article.)

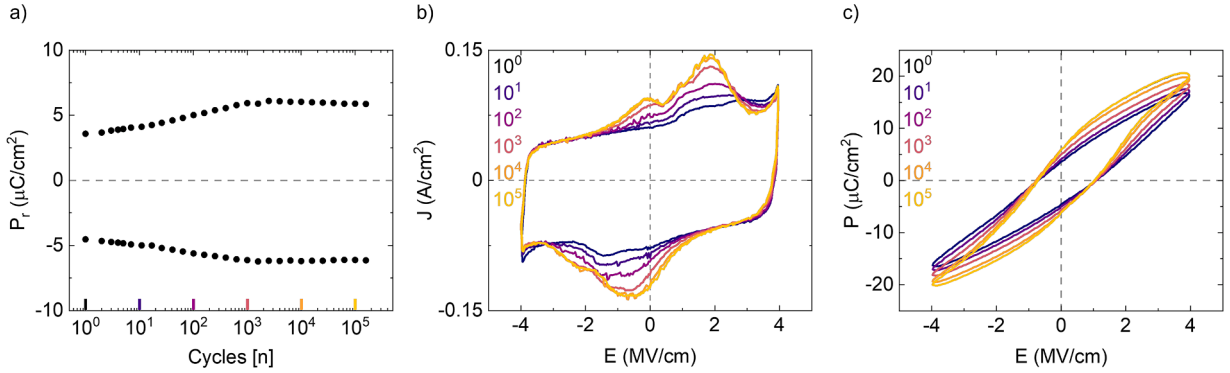

Fig. 5. The endurance test of TiN/HZO/Cr/Au devices. **a)** Remanent polarization P_r measured as a function of the cycle number. **b)** Current density J, and **c)** polarization P as a function of the applied field for selected cycles from a).

selected points from Fig. 5(a), as shown in Fig. 5(b), clear ferroelectric switching peaks are present. We further observe low leakage current contributions in terms of slope of current density and upturns above 3.5 MV/cm, as well as significant dielectric current contributions. For positive bias, the ferroelectric switching current evolves with cycling from two peaks at 1.5 MV/cm and 2.8 MV/cm at the first cycle towards lower switching values of 1 MV/cm and 1.8 MV/cm. There is also a peak appearing at around 0 MV/cm at 10^3 cycles, likely attributable to the appearance of an antiferroelectric phase. For negative bias, the ferroelectric switching current contribution evolves with cycling from two peaks at 0.1 MV/cm and 1.4 MV/cm at the first cycle towards higher switching values of 0.6 MV/cm and 2.2 MV/cm at 10^5 cycles. Such changes in coercive field with cycling have previously been attributed to phase changes in HZO films [46,47]. Lateral and vertical phase content distribution under the electrode will affect the switching current peaks and thus coercive field. For example, two reasons for shifts of coercive field towards lower value could be the appearance of the antiferroelectric orthorhombic phase with a switching peak close to zero field or the reduction of vertical content of ferroelectric orthorhombic phase which lowers the amplitude required for switching and thus the coercive field. To make any further conclusions on the exact phase changes with cycling, a phase- and composition-sensitive nanoprobe operando study would be required.

The change in polarization hysteresis shape with cycling is shown in Fig. 5(c). From the results of PFM, PFS and electrical testing, we conclude that the laser-annealed HZO films are ferroelectric. The remanent polarization obtained in our films (around 6 μC/cm^2) is within the 3–12 μC/cm^2 range reported for other laser-annealed films [22–27] and slightly lower than the 10–25 μC/cm^2 typical values reported for HZO crystallised by conventional RTA [48]. It is worth mentioning that our optimisation of the laser annealing process was based only on the correlation between the laser energy per pulse and the XRD of the films. The ferroelectric characterisation was carried out only in the samples annealed with 4.30 μJ/pulse, but no attempts were made to optimise the preparation of the films by ALD or the laser parameters in terms of polarization. However, we note that a lower $P_r \approx 5$ μC/cm^2 is desirable for some applications because it limits the damage to the nearby layers [49]. Nevertheless, the presence of non-ferroelectric, amorphous regions or tetragonal grains, hardly distinguishable from the orthorhombic ones by XRD, cannot be ruled out.

In the last part of the study, the degree of spatial selectivity of the laser annealing process in the 2D scanning configuration was evaluated. It is important to bear in mind that the energy distribution of the laser beam is Gaussian with a diameter of 80 μm, defined using the $1/e^2$ criterion [50]. Considering the abrupt onset of crystallization observed in Fig. 2, it is reasonable to assume that only the central part of the beam exceeding the threshold fluence contributes to this process, so a laterally narrow transition can be expected.

Although the deflection of the laser beam through galvanometer-controlled mirrors allows the spot to describe arbitrarily complex shapes, we have analysed a simple geometry as a proof of concept. Specifically, we processed only one half of the surface (0.5×1 cm^2 rectangle) in a 1 cm-side square sample, using the optimised laser conditions described previously. The TiN top electrode reflects the light differently from the processed and pristine sides, which could be due to the modification of the surface roughness detected by AFM or the partial oxidation of TiN previously identified by XRD, as was reported before [51,52]. This feature allows the approximate limit separating both regions to be determined by visual inspection.

We examined the crystal structure of the HZO film around this boundary by performing 2θ-scans in nine different positions of the X-ray beam distributed along the X direction perpendicular to the annealing boundary. For these μXRD measurements we ensured the parallel alignment between the apparent boundary (*Y* direction) and the long side of the X-ray beam cross section with an accuracy better than 0.5°. The seven initial micro-diffractograms were measured at intervals of 200 μm. The distance was 400 μm between positions 7 and 8, and 1 mm between positions 8 and 9 in the crystallized side. The μXRD plots measured in these positions are shown in Fig. 6(a). Only the TiN reflection at $2\theta \approx 36.5°$ can be seen in the three initial positions, proving that HZO remains amorphous. By contrast, in the case of positions 5 to 9 the μXRD plots show a very similar shape and reflections at $2\theta = 30.8°$ and $2\theta = 35.6°$, demonstrating that the crystallization of the orthorhombic HZO phase has been completed in the entire volume probed by the X-ray spot. It is worth mentioning that the same HZO reflections are present in position 4 with lower intensity. A concomitant shift of ≈ 0.5° of the TiN peak towards higher angles can be observed here on the processed side of the sample. Fig. 6(b) shows a plot of the integrated area of the line centred at $2\theta = 30.8°$ in all the diffractograms *vs.* the X position (blue circles). The inset of this figure shows a photograph of the sample taken with natural light, on which the positions 1 to 9 are marked.

An additional set of measurements was carried out by fixing the detector at $2\theta = 30.8°$, and then scanning the X position in steps of 50 μm. The resulting normalized μXRD intensity after subtracting the background is plotted in Fig. 6(b) (red circles), superimposed onto the previous integrated areas. As it can be seen, both measurements follow the same trend. The intensity shown in this plot goes from zero to the maximum in ≈ 500 μm, therefore we can conclude that the transition between the amorphous and crystalline region takes place in less than this distance minus the projected size of the X-rays in the *X* direction, that is in ≈ 300 μm. In fact, the true width is likely to be much lower, because even a perfectly steep boundary would be broadened by at least two experimental limitations: (1) the energy distribution across the X-ray beam section is not perfectly flat, and (2) even a 0.5° misalignment of the long side of the X-ray spot relative to the Y axis would further

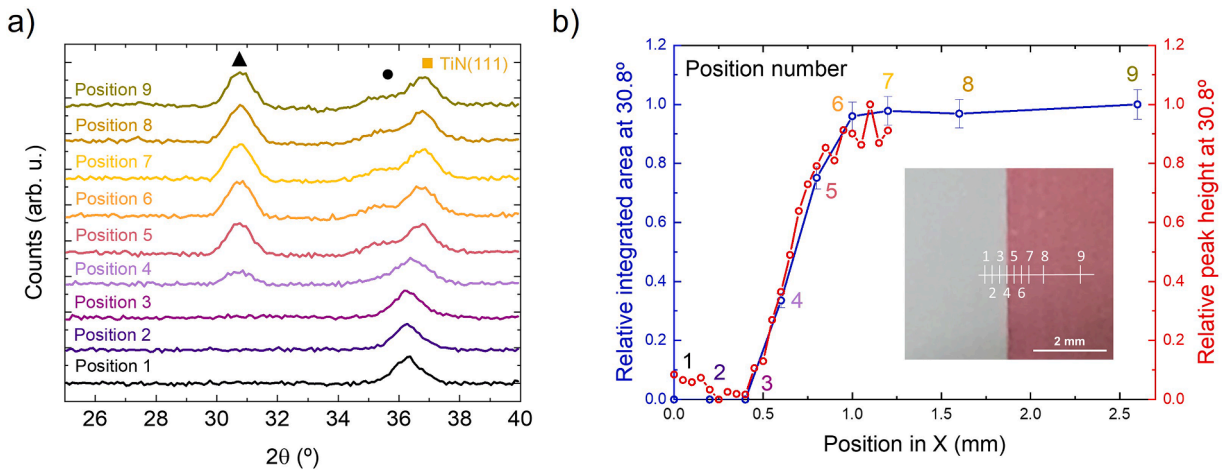

Fig. 6. Analysis of the transition between the non-crystallized (left) and crystallized (right) regions in an HZO film after the partial laser treatment with 4.30 μJ/pulse. **a)** Diffractograms taken at the positions 1–9 along the direction X perpendicular to the boundary. The full triangle shows the expected position of the 101 reflection of the tetragonal phase or the 111 of the polar, orthorhombic phase. **b)** Relative integrated area of the $2\theta = 30.8°$ reflection (blue circles) and relative diffraction intensity (red circles) detected at the same angle, as a function of the position X. Inset: sketch of the positions where the micro-diffraction measurements were taken. (For interpretation of the references to color in this figure legend, the reader is referred to the web version of this article.)

enlarge this apparent size by 90 μm in the 10 mm length of the sample. Overall, these results show the spatially selective transformation by laser crystallisation of amorphous HZO films, with high promise for patterning complex shapes and for the scalability to larger areas.

Finally, we can compare the order of magnitude of the thermal budget between the traditional method and the laser-induced crystallisation analysed here. Conventional middle-temperature annealing requires around 1 min at 600 °C. Considering that twenty films of 1 cm^2 can be processed simultaneously in a 6 kW furnace (a higher number of samples would cause large temperature gradients) and a heating time of 30 min, this gives an energy consumption of 10.8×10^6 J, or 540 kJ per sample. The time needed to anneal one film of the same size using our laser with 8 W of maximum output is 4 min. Given that it has an electrical-to-optical conversion efficiency of ≈10 % (which means 80 W of electrical power), and estimating around 100 W for the laser accessories (cooling system, galvanometer-controlled mirrors, computer, etc.), the overall power of 180 W working for 240 s gives 43.2 kJ per sample. This value is 8 % of the energy consumption using a furnace, confirming that laser annealing is a highly energy-efficient process.

4. Conclusions

Our work demonstrates that amorphous $Hf_{0.5}Zr_{0.5}O_2$ (HZO) thin films deposited between TiN electrodes can be crystallised by sub-nanosecond infrared laser annealing in air atmosphere using a line scanning configuration. In this geometry, a focused laser spot is scanned along a line by means of galvanometer-controlled mirrors so that a homogeneous heat front is defined, which then travels in the perpendicular direction and anneals the sample. In the appropriate range of energy per laser pulse above a threshold value, the HZO films are orthorhombic and ferroelectric.

This strategy had not been explored before (see Table 1) and enables the controlled transformation of selected hafnia regions into the ferroelectric polymorph. Indeed, the micro-diffraction experiments presented here show that the transition between the crystallized and the amorphous region is abrupt within tens of microns. We believe that the use of a laser with ultrashort pulses plays a crucial role in this steep crystallization, as a result of the negligible lateral flow of heat.

Although the experiments described here were performed in simple geometries (either square samples with 1 cm-side length, or in 0.5×1 cm^2 regions of those samples), the laser-annealing method is easily scalable to much larger or smaller sizes, and to arbitrarily complex geometries. It could enable the controlled patterning of submillimetre structures through the spatially selective crystallization. Similar approaches can be found in the literature for a number of materials and applications, such as the writing of electronic circuitry via chemical modification [32], the fabrication of improved pressure sensors using laser microstructuring [53], the direct writing technique based on laser-induced polymerization [54], or the laser crystallisation of perovskite-based LEDs [55]. In addition, the laser is fast, allows high energy savings and is environmentally friendly.

CRediT authorship contribution statement

Alejandro Frechilla: Methodology, Investigation, Resources, Writing – original draft, Writing – review & editing. **Mari Napari:** Methodology, Investigation, Resources, Writing – original draft, Writing – review & editing. **Nives Strkalj:** Methodology, Investigation, Resources, Writing – original draft, Writing – review & editing. **Eduardo Barriuso:** Resources. **Kham Niang:** Resources. **Markus Hellenbrand:** Resources. **Pavel Strichovanec:** Resources. **Firman Mangasa Simanjuntak:** Resources. **Guillermo Antorrena:** Resources. **Andrew Flewitt:** Methodology. **César Magén:** Methodology, Investigation, Writing – original draft, Writing – review & editing. **Germán F. de la Fuente:** Conceptualization, Writing – original draft, Writing – review & editing. **Judith L. MacManus-Driscoll:** Conceptualization, Writing – original draft, Writing – review & editing. **Luis Alberto Angurel:** Conceptualization, Writing – original draft, Writing – review & editing. **José Ángel Pardo:** Conceptualization, Supervision, Writing – original draft, Writing – review & editing.

Declaration of Competing Interest

The authors declare that they have no known competing financial interests or personal relationships that could have appeared to influence the work reported in this paper.

Data availability

Data are available at Zenodo repository under doi: 10.5281/zenodo.10213386.

Acknowledgements

We greatly thank Mary Vickers and Pep Bassas for their technical assistance with the XRD and μXRD experiments. We acknowledge financial support from Spanish Agencia Estatal de Investigación through grants PID2020-112914RB-I00 and PID2020-113034RB-I00 funded by MCIN/AEI/10.13039/501100011033, and from Gobierno de Aragón (research groups T54_23R and E28_23R). A. F. acknowledges support of the Gobierno de Aragón through their predoctoral contracts programme. M. N. acknowledges EPSRC grant EP/P027032/1. The authors acknowledge the use of instrumentation as well as the technical advice provided by the Spanish National Facility ELECMI ICTS, node «Laboratorio de Microscopías Avanzadas (LMA)» at «Universidad de Zaragoza». N. S. acknowledges the Swiss National Science Foundation (grant No. P2EZP2-199913) and the ERC grant EU-H2020-ERC-ADG # 882929, EROS. M. H. gratefully acknowledges funding by the EPSRC and U.S. National Science Foundation with grant EP/T012218/1-ECCS-EPSRC. J.L.M-D. thanks the ERC grant EU-H2020-ERC-ADG # 882929, EROS, and the Royal Academy of Engineering, grant CIET1819_24.

Supplementary materials

Supplementary material associated with this article can be found, in the online version, at doi:10.1016/j.apmt.2023.102033.

References

[1] S. Böscke, J. Müller, D. Bräuhaus, U. Schöder, U. Böttger, Ferroelectricity in hafnium oxide thin films, Appl. Phys. Lett. 99 (2011), 102903, https://doi.org/10.1063/1.3634052.
[2] S.J. Kim, J. Mohan, S.R. Summerfelt, J. Kim, Ferroelectric $Hf_{0.5}Zr_{0.5}O_2$ thin films: a review of recent advances, JOM 71 (2019) 246, https://doi.org/10.1007/s11837-018-3140-5.
[3] U. Schroeder, M.H. Park, T. Mikolajick, C.S. Hwang, The fundamentals and applications of ferroelectric HfO_2, Nat. Rev. Mater. 7 (2022) 653, https://doi.org/10.1038/s41578-022-00431-2.
[4] R. Ruh, H.J. Garrett, R.F. Domagala, N.M. Tallan, The system zirconia-hafnia, J. Am. Ceram. Soc. 51 (1968) 23, https://doi.org/10.1111/j.1151-2916.1968.tb11822.x.
[5] X. Sang, E.D. Grimley, T. Schenk, U. Schroeder, J.M. LeBeau, On the structural origins of ferroelectricity in HfO_2 thin films, Appl. Phys. Lett. 106 (2015), 162905, https://doi.org/10.1063/1.4919135.
[6] M. Hoffmann, U. Schroeder, C. Künneth, A. Kersch, S. Starschich, U. Böttger, T. Mikolajick, Ferroelectric phase transitions in nanoscale HfO_2 films enable giant pyroelectric energy conversion and highly efficient supercapacitors, Nano Energy 18 (2015) 154, https://doi.org/10.1016/j.nanoen.2015.10.005.
[7] M. Pešić, M. Hoffmann, C. Richter, T. Mikolajick, U. Schroeder, Nonvolatile random access memory and energy storage based on antiferroelectric like hysteresis in ZrO_2, Adv. Funct. Mater. 26 (2016) 7486, https://doi.org/10.1002/adfm.201603182.
[8] T. Mittmann, F.P.G. Fengler, C. Richter, M.H. Park, T. Mikolajick, U. Schroeder, Optimizing process conditions for improved $Hf_{1-x}Zr_xO_2$ ferroelectric capacitor performance, Microelectron. Eng. 178 (2017) 48, https://doi.org/10.1016/j.mee.2017.04.031.
[9] T. Mikolajick, S. Slesazeck, M.H. Park, U. Schroeder, Ferroelectric hafnium oxide for ferroelectric random-access memories and ferroelectric field-effect transistors, MRS Bull. 43 (2018) 340, https://doi.org/10.1557/mrs.2018.92.
[10] L. Chen, T.-Y. Wang, Y.-W. Dai, M.-Y. Cha, H. Zhu, Q.-Q. Sun, S.-J. Ding, P. Zhou, L. Chua, D.W. Zhang, Ultra-low power $Hf_{0.5}Zr_{0.5}O_2$ based ferroelectric tunnel junction synapses for hardware neural network applications, Nanoscale 10 (2018) 15826, https://doi.org/10.1039/C8NR04734K.
[11] B. Hanrahan, C. Mart, T. Kämpfe, M. Czernohorsky, W. Weinreich, A. Smith, Pyroelectric energy conversion in doped hafnium oxide (HfO_2) thin films on area-enhanced substrates, Energy Technol. 7 (2019), 1900515, https://doi.org/10.1039/C8NR04734K.
[12] F. Cüppers, S. Menzel, C. Bengel, A. Hardtdegen, M. von Witzleben, U. Böttger, R. Waser, S. Hoffmann-Eifert, Exploiting the switching dynamics of HfO_2-based ReRAM devices for reliable analog memristive behaviour, APL Mater. 7 (2019), 091105, https://doi.org/10.1063/1.5108654.
[13] E.T. Breyer, H. Mulaosmanovic, T. Mikolajick, S. Slesazeck, Perspective on ferroelectric, hafnium oxide based transistors for digital beyond von-Neumann computing, Appl. Phys. Lett. 118 (2021), 050501, https://doi.org/10.1063/5.0035281.
[14] M. Hoffmann, S. Salahuddin, Ferroelectric gate oxides for negative capacitance transistors, MRS Bull. 46 (2021) 930, https://doi.org/10.1557/s43577-021-00208-y.
[15] M.L. Müller, M.T. Becker, N. Strkalj, J.L. MacManus-Driscoll, Schottky-to-Ohmic switching in ferroelectric memristors based on semiconducting $Hf_{0.93}Y_{0.07}O_2$ thin films, Appl. Phys. Lett. 121 (2022), 093501, https://doi.org/10.1063/5.0095762.
[16] J.Y. Park, D.-H. Choe, D.H. Lee, G.T. Yu, K. Yang, S.H. Kim, G.H. Park, S.-G. Nam, H.J. Lee, S. Jo, B.J. Kuh, D. Ha, Y. Kim, J. Heo, M.H. Park, Revival of ferroelectric memories based on emerging fluorite-structured ferroelectrics, Adv. Mater. 35 (2023) 2204904, https://doi.org/10.1002/adma.202204904.
[17] S. Migita, H. Ota, K. Shibuya, H. Yamada, A. Sawa, T. Matsukawa, A. Toriumi, Phase transformation behavior of ultrathin $Hf_{0.5}Zr_{0.5}O_2$ films investigated through wide range annealing experiments, Jpn. J. Appl. Phys. 58 (2019) SBBA07, https://doi.org/10.7567/1347-4065/ab00f6.
[18] H.A. Hsain, Y. Lee, M. Materano, T. Mittmann, A. Payne, T. Mikolajick, U. Schroeder, G.N. Parsons, J.L. Jones, Many routes to ferroelectric HfO_2: a review of current deposition methods featured, J. Vac. Sci. Technol. A 40 (2022), 010803, https://doi.org/10.1116/6.0001317.
[19] E. O'Connor, M. Halter, F. Eltes, M. Sousa, A. Kellock, S. Abel, J. Fompeyrine, Stabilization of ferroelectric $Hf_xZr_{1-x}O_2$ films using a millisecond flash lamp annealing technique, APL Mater. 6 (2018), 121103, https://doi.org/10.1063/1.5060676.
[20] H. Tanimura, Y. Ota, H. Kawarazaki, S. Kato, T. Nara, Fabrication of thin ferroelectric $Hf_{0.5}Zr_{0.5}O_2$ films by millisecond flash lamp annealing, Jpn. J. Appl. Phys. 62 (2023) SC1044, https://doi.org/10.35848/1347-4065/acb1b7.
[21] T. Tabata, Nucleation and crystal growth in HfO_2 thin films by UV nanosecond pulsed laser annealing, Appl. Phys. Express 13 (2020), 015509, https://doi.org/10.7567/1882-0786/ab5ce2.
[22] L. Grenouillet, T. Francois, J. Coignus, S. Kerdilès, N. Vaxelaire, C. Carabasse, F. Mehmood, S. Chevalliez, C. Pellissier, F. Triozon, F. Mazen, G. Rodriguez, T. Magis, V. Havel, S. Slesazeck, F. Gaillard, U. Schroeder, T. Mikolajick, E. Nowak, Nanosecond laser anneal (NLA) for Si-implanted HfO_2 ferroelectric memories integrated in back-end of line (BEOL), Proceedings of the 2020 Symposium on VLSI Technology (2020), https://doi.org/10.1109/VLSITechnology18217.2020.9265061.
[23] N. Volodina, A. Dmitriyeva, A. Chouprik, E. Gatskevich, A. Zenkevich, Ferroelectric $Hf_{0.5}Zr_{0.5}O_2$ thin films crystallized by pulsed laser annealing, Phys. Status Solidi RRL 15 (2021), 2100082, https://doi.org/10.1002/pssr.202100082.
[24] T. Tabata, S. Halty, F. Rozé, K. Huet, F. Mazzamuto, Non-doped HfO_2 crystallization controlled by dwell time in laser annealing, Appl. Phys. Express 14 (2021), 115503, https://doi.org/10.35848/1882-0786/ac2c18.
[25] T. Ali, R. Olivo, S. Kerdilès, D. Lehninger, M. Lederer, D. Sourav, A.-S. Royet, A. Sünbül, A. Prabhu, K. Kühnel, M. Czernohorsky, M. Rudolph, R. Hoffmann, C. Charpin-Nicolle, L. Grenouillet, T. Kämpfe, K. Seidel, Study of nanosecond laser annealing on silicon doped hafnium oxide film crystallization and capacitor reliability, Proceedings of the 2022 IEEE International Memory Workshop (2022), https://doi.org/10.1109/IMW52921.2022.9779281.
[26] A.P.S. Crema, M.C. Istrate, A. Silva, V. Lenzi, L. Domingues, M.O. Hill, V. S. Teodorescu, C. Ghica, M.J.M. Gomes, M. Pereira, L. Marques, J.L. MacManus-Driscoll, J.P.B. Silva, Ferroelectric orthorhombic ZrO_2 thin films achieved through nanosecond laser annealing, Adv. Sci. (2023), 2207390, https://doi.org/10.1002/advs.202207390.
[27] M.S. Song, K. Park, K. Lee, J.W. Cho, T.Y. Lee, J. Park, S.C. Chae, Selective crystallization of ferroelectric $Hf_xZr_{1-x}O_2$ via excimer laser annealing, ACS Appl. Electron. Mater. 5 (2023) 117, https://doi.org/10.1021/acsaelm.2c01555.
[28] S. Kang, W.-S. Jang, A.N. Morozovska, O. Kwon, Y. Jin, Y.-H. Kim, H. Bae, C. Wang, S.-H. Yang, A. Belianinov, S. Randolph, E.A. Eliseev, L. Collins, Y. Park, S. Jo, M.-H. Jung, K.-J. Go, H.W. Cho, S.-Y. Choi, J.H. Jang, S. Kim, H.Y. Jeong, J. Lee, O. S. Ovchinnikova, J. Heo, S.V. Kalinin, Y.-M. Kim, Y. Kim, Highly enhanced ferroelectricity in HfO_2-based ferroelectric thin film by light ion bombardment, Science 376 (2022) 731, https://doi.org/10.1126/science.abk3195.
[29] R. Le Harzic, N. Huot, E. Audouard, C. Jonin, P. Laporte, S. Valette, A. Fraczkiewicz, R. Fortunier, Comparison of heat-affected zones due to nanosecond and femtosecond laser pulses using transmission electronic microscopy, Appl. Phys. Lett. 80 (2002) 3886, https://doi.org/10.1063/1.1481195.
[30] Z. Chuanchao, Z. Lijuan, J. Xiaolong, J. Baoshen, L. Wei, D. Rucheng, C. Jing, Y. Xiaodong, J. Xiaodong, Influence of pulse length on heat affected zones of evaporatively-mitigated damages of fused silica optics by CO_2 laser, Opt. Lasers Eng. 125 (2020), 105857, https://doi.org/10.1016/j.optlaseng.2019.105857.
[31] R. Nakajima, M. Abe, Y. Benino, T. Fujiwara, H.G. Kim, T. Komatsu, Laser-induced crystallization of β'-$RE_2(MoO_4)_3$ ferroelectrics (RE: sm, Gd, Dy) in glasses and their surface morphologies, J. Non Cryst. Solids 353 (2007) 85, https://doi.org/10.1016/j.jnoncrysol.2006.08.050.
[32] D. Austin, K. Gliebe, C. Muratore, B. Boyer, T.S. Fisher, L.K. Beagle, A. Benton, P. Look, D. Moore, E. Ringe, B. Treml, A. Jawaid, R. Vaia, W.J. Kennedy, P. Buskohl, N.R. Glavin, Laser writing of electronic circuitry in thin film molybdenum disulfide: a transformative manufacturing approach, Mater. Today 43 (2021) 17, https://doi.org/10.1016/j.mattod.2020.09.036.
[33] L.C. Estepa, G.F. de la Fuente: Continuous furnace with coupled laser for the surface treatment of materials", European Patent EP1992445 (2008), US Patent 20090230105 (2009), China Patent No. ZL 2012100224412, 2014.
[34] X.F. de la Fuente Leis, L.C. Estepa Millán, L. A. Angurel Lambán: "Method for modifying a vitreous material". Patent WO2021176123A1.
[35] V. Lennikov, B. Özkurt, L.A. Angurel, A. Sotelo, B. Özçelik, G.F. de la Fuente, Microstructure and transport properties of Bi-2212 prepared by CO_2 laser line scanning, J. Superconduct. Novel Magn. 26 (2013) 947, https://doi.org/10.1007/s10948-012-1934-1.

[36] L. Porta-Velilla, N. Turan, Á. Cubero, W. Shao, H. Li, G.F. de la Fuente, E. Martínez, Á. Larrea, M. Castro, H. Koralay, S. Çavdar, J. Bonse, L.A. Angurel, "Highly regular hexagonally-arranged nanostructures on Ni-W alloy tapes upon irradiation with ultrashort UV laser pulses, Nanomaterials 12 (2022) 2380, https://doi.org/10.3390/nano12142380.

[37] M. Hasegawa, T. Yagi, Systematic study of formation and crystal structure of 3d-transition metal nitrides synthesized in a supercritical nitrogen fluid under 10 GPa and 1800 K using diamond anvil cell and YAG laser heating, J. Alloys Compd. 403 (2005) 131, https://doi.org/10.1016/j.jallcom.2005.04.197.

[38] J. Bonse, J. Krüger, Probing the heat affected zone by chemical modifications in femtosecond pulse laser ablation of titanium nitride films in air, J. Appl. Phys. 107 (2010), 054902, https://doi.org/10.1063/1.3311552.

[39] M. Jafari, L. Rogström, J.M. Andersson, J. Birch, J. Gibmeier, M.J. Jöesaar, D. Kiefer, M. Odén, Thermal degradation of TiN and TiAlN coatings during rapid laser treatment, Surf. Coat. Technol. 422 (2021), 127517, https://doi.org/10.1016/j.surfcoat.2021.127517.

[40] W. Hamouda, A. Pancotti, C. Lubin. L. Tortech, C. Richter. T. Mikolajick. U. Schroeder, N. Barrett, Physical chemistry of the TiN/$Hf_{0.5}Zr_{0.5}O_2$ interface, J. Appl. Phys. 127 (2020), 064105, https://doi.org/10.1063/1.5128502.

[41] E.O. Filatova, A.S. Konashuk, S.S. Sakhonenkov, A.U. Gaisin, N.M. Kolomiiets, V. V. Afanas'ev, H.F.W. Dekkers, Mechanisms of TiN Effective Workfunction Tuning at Interfaces with HfO_2 and SiO_2, J. Phys. Chem. C 124 (2020) 15547, https://doi.org/10.1021/acs.jpcc.0c03605.

[42] M. Müller, P. Lömker, P. Rosenberger, M.H. Hamed, D.N. Mueller, R.A. Heinen, T. Szyjka, L. Baumgarten, Hard x-ray photoelectron spectroscopy of tunable oxide interfaces, J. Vac. Sci. Technol. A 40 (2022), 013215, https://doi.org/10.1116/6.0001491.

[43] S. Bartkowski, M. Neumann, E.Z. Kurmaev, V.V. Fedorenko, S.N. Shamin, V. M. Cherkashenko, S.N. Nemnonov, A. Winiarski, D.C. Rubie, Electronic structure of titanium monoxide, Phys. Rev. B 56 (1997), 10656, https://doi.org/10.1103/PhysRevB.56.10656.

[44] F. El Kamel, P. Gonon, C. Vallée, C. Jorel, Electrode effects on the conduction mechanisms in HfO_2-based metal-insulator-metal capacitors, J. Appl. Phys. 106 (2009), 064508, https://doi.org/10.1063/1.3226857.

[45] N. Balke, P. Maksymovych, S. Jesse, A. Herklotz, A. Tselev, C.-B. Eom, I. I. Kravchenko, P. Yu, S.V. Kalinin, Differentiating ferroelectric and nonferroelectric electromechanical effects with scanning probe microscopy, ACS Nano 9 (2015) 6484, https://doi.org/10.1021/acsnano.5b02227.

[46] S.R.C. McMitchell, S. Clima, N. Ronchi, K. Banerjee, U. Celano, M. Popovici, L. Di Piazza, G. Van den Bosch, J. Van Houdt, Elucidating possible crystallographic origins of wake-up mechanisms in ferroelectric hafnia, Appl. Phys. Lett. 118 (2021), 092902, https://doi.org/10.1063/5.0029691.

[47] A. Jan, T. Rembert, S. Taper, J. Symonowicz, N. Strkalj, T. Moon, Y. Seong Lee, H. Bae, H.J. Lee, D.-H. Choe, J. Heo, J. MacManus-Driscoll, B. Monserrat, G. Di Martino, In operando optical tracking of oxygen vacancy migration and phase change in few nanometers ferroelectric HZO memories, Adv. Funct. Mater. 2023 (2023), 2214970, https://doi.org/10.1002/adfm.202214970.

[48] M.H. Park, D.H. Lee, K. Yang, J.-Y. Park, G.T. Yu, H.W. Park, M. Materano, T. Mittmann, P.D. Lomenzo, T. Mikolajick, U. Schroeder, C.S. Hwang, Review of defect chemistry in fluorite-structure ferroelectrics for future electronic devices, J. Mater. Chem. C 8 (2020) 10526, https://doi.org/10.1039/D0TC01695K.

[49] H. Mulaosmanovic, E.T. Breyer, S. Dünkel, S. Beyer, T. Mikolajick, S. Slesazeck, Ferroelectric field-effect transistors based on HfO_2: a review, Nanotechnology 32 (2021), 502002, https://doi.org/10.1088/1361-6528/ac189f.

[50] J.M. Liu, Simple technique for measurements of pulsed Gaussian-beam spot sizes, Opt. Lett. 7 (1982) 196, https://doi.org/10.1364/OL.7.000196.

[51] A. Scherbak, O. Yulmetova, Contrast image formation based on thermodynamic approach and surface laser oxidation process for optoelectronic read-out system, Opt. Laser Technol. 101 (2018) 242, https://doi.org/10.1016/j.optlastec.2017.11.030.

[52] H.A. Abd El-Fattah, I.S. El-Mahallawi, M.H. Shazly, W.A. Khalifa, Optical Properties and microstructure of TiN_xO_y and TiN thin films before and after annealing at different conditions, Coatings 9 (2019) 22, https://doi.org/10.3390/coatings9010022.

[53] Y. Gao, C. Lu, Y. Guohui, J. Sha, J. Tan, F. Xuan, Laser micro-structured pressure sensor with modulated sensitivity for electronic skins, Nanotechnology 30 (2019), 325502, https://doi.org/10.1088/1361-6528/ab1a86.

[54] S. Kawata, H.-B. Sun, T. Tanaka, K. Takada, Finer features for functional microdevices, Nature 412 (2001) 697, https://doi.org/10.1038/35089130.

[55] S.J. Kim, J. Byun, T. Jeon, H.M. Jin, H.R. Hong, S.O. Kim, Perovskite light-emitting diodes via laser crystallization: systematic investigation on grain size effects for device performance, ACS Appl. Mater. Interfaces 10 (2018) 2490, https://doi.org/10.1021/acsami.7b15470.